

Chemical Non-Equilibrium Reentry Flows in Two-Dimensions – Part I

EDISSON SÁVIO DE GÓES MACIEL AND AMILCAR PORTO PIMENTA

IEA – Aeronautical Engineering Division

ITA – Aeronautical Technological Institute

Praça Mal. Eduardo Gomes, 50 – Vila das Acácias – São José dos Campos – SP – 12228-900

BRAZIL

edisavio@edissonsavio.eng.br and amilcar@ita.br

Abstract: - This work presents a numerical tool implemented to simulate inviscid and viscous flows employing the reactive gas formulation of thermal equilibrium and chemical non-equilibrium. The Euler and Navier-Stokes equations, employing a finite volume formulation, on the context of structured and unstructured spatial discretizations, are solved. The aerospace problem involving the hypersonic flow around a blunt body, in two-dimensions, is simulated. The reactive simulations will involve an air chemical model of five species: N, N₂, NO, O and O₂. Seventeen chemical reactions, involving dissociation and recombination, will be simulated by the proposed model. The algorithm employed to solve the reactive equations was the Van Leer, first- and second-order accurate ones. The second-order numerical scheme is obtained by a “MUSCL” (Monotone Upstream-centered Schemes for Conservation Laws) extrapolation process in the structured case. The algorithm is accelerated to the steady state solution using a spatially variable time step procedure, which has demonstrated effective gains in terms of convergence rate, as reported in Maciel. The results have demonstrated that the most correct aerodynamic coefficient of lift is obtained by the Van Leer first-order accurate scheme in the inviscid, structured, blunt body simulation. Moreover, the shock position is closer to the geometry as using the reactive formulation than the ideal gas formulation. It was verified in the inviscid and viscous cases.

Key-Words: - Euler and Navier-Stokes equations, Chemical non-equilibrium, Five species model, Hypersonic flow, Van Leer algorithm.

1 Introduction

In several aerodynamic applications, the atmospheric air, even being composed of several chemical species, can be considered as a perfect thermal and caloric gas due to its inert property as well its uniform composition in space and constancy in time. However, there are several practical situations involving chemical reactions, as for example: combustion processes, flows around aerospace vehicles in reentry conditions or plasma flows, which do not permit the ideal gas hypothesis ([1]). As described in [2], since these chemical reactions are very fast such that all processes can be considered in equilibrium, the conservation laws which govern the fluid become essentially unaltered, except that one equation to the general state of equilibrium has to be used opposed to the ideal gas law. When the flow is not in chemical equilibrium, one mass conservation law has to be written to each chemical species and the size of the equation system increases drastically.

Hypersonic flows are primary characterized by a very high level of energy ([3]). Through the shock wave, the kinetic energy is transformed in enthalpy. The flow temperature between the shock wave and the body is very high. Under such conditions, the air

properties are considerably modified. Phenomena like vibrational excitation and molecular dissociation of O₂ and N₂ frequently occur. The energy is stored under a form of free energy and the flow temperature is extremely reduced as compared with the temperature of an ideal gas flow. The thermodynamic and transport coefficients are not more constants. In summary, the ideal gas hypothesis is not truer and such flow is called the hypersonic flow of reactive gas or “hot gas flow”.

During the reentry and the hypersonic flights of aerospace vehicles in the atmosphere, reactive gas effects are present. The analysis of such hypersonic flows is critical to an appropriated aerodynamic and thermal project of such vehicles. The numerical simulation of reactive-gas-hypersonic flows is a very complex and disputed task. The present work emphasizes the numerical simulation of hypersonic flow in thermal equilibrium and chemical non-equilibrium.

This work, the first part of this study, presents a numerical tool implemented to simulate inviscid and viscous flows employing the reactive gas formulation of thermal equilibrium and chemical non-equilibrium flow in two-dimensions. The Euler and Navier-Stokes equations, employing a finite volume formulation, on the context of structured

and unstructured spatial discretizations, are solved. These variants allow an effective comparison between the two types of spatial discretization aiming verify their potentialities: solution quality, convergence speed, computational cost, etc. The aerospace problem involving the “hot gas” hypersonic flow around a blunt body, in two-dimensions, is simulated. The algorithm is accelerated to the steady state solution using a spatially variable time step procedure, which has demonstrated effective gains in terms of convergence rate, as shown in [4-5].

In this work, first part of this study, the structured formulation of the two-dimensional Euler and Navier-Stokes reactive equations is presented. In a next paper, the second part of this study, it will be presented the unstructured version of the calculation algorithm in two-dimensions to complete the formulation in structured and in unstructured contexts. However, solutions to the structured and unstructured cases are presented in both papers.

The reactive simulations will involve an air chemical model of five species: N, N₂, NO, O and O₂. Seventeen chemical reactions, involving dissociation and recombination, will be simulated by the proposed model. The Arrhenius formula will be employed to determine the reaction rates and the law of mass action will be used to determine the source terms of each gas species equation.

The algorithm employed to solve the reactive equations was the [6], first- and second-order accurate ones. The second-order numerical scheme is obtained by a MUSCL extrapolation process in the structured case (details in [7]). In the unstructured case, tests with the linear reconstruction process (details in [8]) did not yield converged results and, therefore, were not presented. The algorithm was implemented in a FORTRAN programming language, using the software Microsoft Developer Studio. Simulations in three microcomputers (one desktop and two notebooks) were accomplished: one with processor Intel Celeron of 1.5 GHz of clock and 1.0 GBytes of RAM (notebook), one with processor AMD-Sempron of 1.87 GHz of clock and 512 MBytes of RAM (desktop) and the third one with processor Intel Celeron of 2.13 GHz of clock and 1.0 GBytes of RAM (notebook).

The results have demonstrated that the most correct aerodynamic coefficient of lift is obtained by the [6] first-order accurate scheme in the inviscid, structured, blunt body simulation. The cheapest algorithm was the unstructured [6] scheme, first-order accurate in space, to an inviscid simulation.

Moreover, the shock position is closer to the geometry as using the reactive formulation than the ideal gas formulation. It was verified in the inviscid and viscous cases.

As the consequence of such study, a three-dimensional work, [23], following this one has been performed. [23] work has presented a numerical tool implemented to simulate inviscid and viscous flows employing the reactive gas formulation of thermal equilibrium and chemical non-equilibrium in three-dimensions. The aerospace problem involving the hypersonic flow around a blunt body, in three-dimensions, was simulated. The present paper is similar to [23], but is different in terms of spatial solution. The former shows two-dimensional solutions of the flow around a blunt body, whereas the latter shows three-dimensional solutions of the flow around a blunt body configuration. Both works are applied to solve the Euler and Navier-Stokes equations, in each spatial system, and both works solved a five (5) species chemical model, involving seventeen (17) chemical reactions, using the Arrhenius formula and the law of mass action to solve the chemical part. Although they seems very similar, both works were applied to different spatial dimensions, where in the three-dimensional case, due to the third dimension, a closer shock wave is captured than its two-dimensional counterpart. So, the third dimension shows a significant influence in the solution quality, differing from the present work.

2 Formulation to Reactive Flow in Thermal Equilibrium and Chemical Non-Equilibrium

2.1 Reactive equations in two-dimensions

The Navier-Stokes equations in thermal equilibrium and chemical non-equilibrium were implemented on a finite volume context, in the two-dimensional space. In this space, such equations in integral and conservative forms can be expressed by:

$$\frac{\partial}{\partial t} \int_V Q dV + \int_S \vec{F} \cdot \vec{n} dS = \int_V S_C dV, \text{ with:}$$

$$\vec{F} = (E_e - E_v) \vec{i} + (F_e - F_v) \vec{j}, \quad (1)$$

where: Q is the vector of conserved variables, V is the computational cell volume, \vec{F} is the complete flux vector, \vec{n} is the normal unity vector to the flux face, S is the flux area, S_C is the chemical source

term, E_e and F_e are the convective flux vectors or the Euler flux vectors in the x and y directions, respectively, and E_v and F_v are the viscous flux vectors in the x and y directions, respectively. The \vec{i} and \vec{j} unity vectors define the Cartesian coordinate system. Eight (8) conservation equations are solved: one of general mass conservation, two of linear momentum conservation, one of total energy and four of species mass conservation. Therefore, one of the species is absent of the iterative process. The CFD (Computational Fluid Dynamics) literature recommends that the species to be omitted of the formulation should be that of biggest mass fraction of the gaseous mixture, aiming to result in the minimum accumulated numerical error, corresponding to the major constituent of the mixture (in the case, air). To the present study, in which is chosen an air chemical model composed of five (5) chemical species (N, N₂, NO, O and O₂) and seventeen (17) chemical reactions, being fifteen (15) dissociation reactions (endothermic reactions), this species can be the N₂ or the O₂. To this work, the O₂ was the chosen species. The Q , E_e , F_e , E_v , F_v and S_C vectors can, hence, be defined conform below ([3]):

$$Q = \begin{Bmatrix} \rho \\ \rho u \\ \rho v \\ e \\ \rho_1 \\ \rho_2 \\ \rho_3 \\ \rho_4 \end{Bmatrix}, E_e = \begin{Bmatrix} \rho u \\ \rho u^2 + p \\ \rho uv \\ \rho H u \\ \rho_1 u \\ \rho_2 u \\ \rho_3 u \\ \rho_4 u \end{Bmatrix}, F_e = \begin{Bmatrix} \rho v \\ \rho uv \\ \rho v^2 + p \\ \rho H v \\ \rho_1 v \\ \rho_2 v \\ \rho_3 v \\ \rho_4 v \end{Bmatrix},$$

$$E_v = \frac{1}{Re} \begin{Bmatrix} 0 \\ \tau_{xx} \\ \tau_{xy} \\ \tau_{xx}u + \tau_{xy}v - q_x - \phi_x \\ -\rho_1 v_{1x} \\ -\rho_2 v_{2x} \\ -\rho_3 v_{3x} \\ -\rho_4 v_{4x} \end{Bmatrix},$$

$$F_v = \frac{1}{Re} \begin{Bmatrix} 0 \\ \tau_{xy} \\ \tau_{yy} \\ \tau_{xy}u + \tau_{yy}v - q_y - \phi_y \\ -\rho_1 v_{1y} \\ -\rho_2 v_{2y} \\ -\rho_3 v_{3y} \\ -\rho_4 v_{4y} \end{Bmatrix}, \quad (2)$$

$$S_C = \{0 \ 0 \ 0 \ 0 \ \dot{\omega}_1 \ \dot{\omega}_2 \ \dot{\omega}_3 \ \dot{\omega}_4\}^T, \quad (3)$$

where: ρ is the mixture density; u and v are the Cartesian velocity components in the x and y directions, respectively; p is the fluid static pressure; e is the fluid total energy; ρ_1 , ρ_2 , ρ_3 and ρ_4 are the densities of the N, N₂, NO and O, respectively; H is the total enthalpy of the mixture; the τ 's are the components of the viscous stress tensor; q_x and q_y are the components of the Fourier heat flux vector in the x and y directions, respectively; Re is the laminar Reynolds number of the flow; $\rho_s v_{sx}$ and $\rho_s v_{sy}$ represent the diffusion flux of the species, defined according to the Fick law; ϕ_x and ϕ_y are the terms of mixture diffusion; and $\dot{\omega}_s$ is the chemical source term of each species equation, defined by the law of mass action.

The viscous stresses, in N/m², are determined, following a Newtonian fluid model, by:

$$\begin{aligned} \tau_{xx} &= 2\mu \frac{\partial u}{\partial x} - \frac{2}{3}\mu \left(\frac{\partial u}{\partial x} + \frac{\partial v}{\partial y} \right), \\ \tau_{xy} &= \mu \left(\frac{\partial u}{\partial y} + \frac{\partial v}{\partial x} \right), \\ \tau_{yy} &= 2\mu \frac{\partial v}{\partial y} - \frac{2}{3}\mu \left(\frac{\partial u}{\partial x} + \frac{\partial v}{\partial y} \right), \end{aligned} \quad (4)$$

in which μ is the fluid molecular viscosity. The components of the Fourier heat flux vector, which considers only thermal conduction, are defined by:

$$q_x = -k \frac{\partial T}{\partial x} \quad \text{and} \quad q_y = -k \frac{\partial T}{\partial y}. \quad (5)$$

The laminar Reynolds number is defined by:

$$Re = \rho_\infty V_\infty L / \mu_\infty, \quad (6)$$

where “ ∞ ” represents freestream properties, V_∞ represents the flow characteristic velocity and L is a characteristic length of the studied configuration. The species diffusion terms, defined by the Fick law, to a thermal equilibrium condition, are determined by ([3]):

$$\rho_s v_{sx} = -\rho D \frac{\partial Y_s}{\partial x} \quad \text{and} \quad \rho_s v_{sy} = -\rho D \frac{\partial Y_s}{\partial y}, \quad (7)$$

with “ s ” referent to a given species, Y_s being the species mass fraction and D the binary diffusion coefficient of the mixture. The chemical species mass fraction “ Y_s ” is defined by:

$$Y_s = \rho_s / \rho \quad (8)$$

and the binary diffusion coefficient of the mixture is defined by:

$$D = \frac{kLe}{\rho Cp}, \quad (9)$$

where: k is the mixture thermal conductivity; Le is the Lewis number, kept constant to thermal equilibrium, with value 1.4; and Cp is the mixture specific heat at constant pressure. The Cp calculation is presented in section 2.2. The ϕ_x and ϕ_y diffusion terms which appear in the energy equation are determined by ([3]):

$$\phi_x = \sum_{s=1}^{ns} \rho_s v_{sx} h_s \quad \text{and} \quad \phi_y = \sum_{s=1}^{ns} \rho_s v_{sy} h_s, \quad (10)$$

being v_{sx} and v_{sy} the species diffusion velocities in the x and y directions, respectively; h_s the specific enthalpy (sensible) of the chemical species “ s ” and “ ns ” the total number of chemical species.

2.2 Thermodynamic model/Thermodynamic properties

To a thermal equilibrium and chemical non-equilibrium formulation, it was necessary the specification of the specific heat at constant pressure and of the specific enthalpy. According to [9], the expressions to these quantities were estimated conform below:

$$\frac{Cp_s}{R_{univ}} = A_1 + A_2 T + A_3 T^2 + A_4 T^3 + A_5 T^4, \quad (11)$$

where: Cp_s is the specific heat at constant pressure to the “ s ” species; R_{univ} is the gas universal constant [$R_{univ} = 8,314.3 \text{ J}/(\text{kg}\cdot\text{mol}\cdot\text{K}) = 1.987 \text{ cal}/(\text{g}\cdot\text{mol}\cdot\text{K})$, $1 \text{ cal} = 4.184 \text{ J}$]; The A_1 , A_2 , A_3 , A_4 and A_5 are coefficients of curve adjust to several temperature ranges, given in [9-10]; T is the absolute mixture temperature, given in Kelvin.

The specific enthalpy (sensible enthalpy) is given by the following expression:

$$\frac{h_s}{R_{univ} T} = A_1 + \frac{A_2 T}{2} + \frac{A_3 T^2}{3} + \frac{A_4 T^3}{4} + \frac{A_5 T^4}{5} + \frac{A_6}{T}, \quad (12)$$

where: A_1 , A_2 , A_3 , A_4 , A_5 and A_6 are coefficients of curve adjust to several temperature ranges. The values of these coefficients are presented in [9-10]. Aiming to smooth the behavior of the thermodynamic properties at the boundaries of each interval, [9-10] presents a subroutine list which performs linear interpolation of such thermodynamic curves in appropriated intervals. In such manner, it is possible to avoid the discontinuity of the first derivative of the thermodynamic properties in relation to the temperature, obtaining, of this way, smooth functions in all the interval of the curve adjust. The mixture total energy is determined by:

$$e = \rho \left[\sum_{s=1}^{ns} Y_s C_{v_s} T + \sum_{s=1}^{ns} Y_s h_s^0 + 1/2 (u^2 + v^2) \right], \quad (13)$$

in the two-dimensional case,

where:

C_{v_s} is the specific heat at constant volume to each “ s ” chemical species, in $\text{J}/(\text{kg}\cdot\text{K})$;

$$C_{v_s} = 3/2 R_s, \quad (14)$$

to monatomic gas, in $\text{J}/(\text{kg}\cdot\text{K})$;

$$C_{v_s} = 5/2 R_s, \quad (15)$$

to diatomic gas, in $\text{J}/(\text{kg}\cdot\text{K})$;

$$R_s = R_{univ} / M_s, \quad (16)$$

gas specific constant of the “ s ” chemical species, in $\text{J}/(\text{kg}\cdot\text{K})$;

M_s is the molecular weight of the “ s ” species;

T is the translational/rotational temperature;

$$h_s^0 = \sum_{s=1}^{ns} Y_s h_s^0 \quad (17)$$

is the mixture formation enthalpy.

h_s^0 is the formation enthalpy of each “ s ” chemical species (with value 0.0 to diatomic gases of the

same species). The species-formation enthalpy per g-mol of the species is shown in Table 1.

Table 1 : Species-formation enthalpy.

S ⁽¹⁾	N	N ₂	NO	O	O ₂
h ⁰⁽²⁾	470,816.0	0.0	90,671.0	0.0	246,783.0

⁽¹⁾ S = Species; ⁽²⁾ Given in J/g-mol.

As can be observed, dividing each term above by the species molecular weight and multiplying the result by 10³, it is possible to obtain the formation enthalpy in J/kg. The mixture sensible enthalpy, the mixture specific heat at constant pressure, the density of each chemical species “s” and the principle of conservation of the mixture mass fraction are defined by:

$$h = \sum_{s=1}^{ns} Y_s h_s, \quad C_p = \sum_{s=1}^{ns} Y_s C_{p_s};$$

$$\rho = \sum_{s=1}^{ns} Y_s \rho_s = \sum_{s=1}^{ns} \rho_s \Leftrightarrow \rho_s = Y_s \rho,$$

$$\sum_{s=1}^{ns} Y_s = 1, \quad (18)$$

where: C_{p_s} is the specific heat at constant pressure of the “s” chemical species. The mixture total enthalpy is determined by:

$$H = h + 0.5(u^2 + v^2), \quad (19)$$

in the two-dimensional case.

As the system of equations is solved to “ns-1” species, the density of the nth species is determined by:

$$\rho_n = \rho - \sum_{s=1}^{ns-1} \rho_s. \quad (20)$$

The species molecular weights in g/g-mol are obtained from [11] and are presented in Table 2.

To the case of thermal equilibrium and chemical non-equilibrium, it is common in the CFD literature the reference to a frozen ratio of specific heats to be calculation of the sound speed. This ratio is defined as follows. First, the mixture specific heat at constant pressure and the mixture specific heat at constant volume are calculated:

$$C_{p_{mixt}} = \sum_{s=1}^{ns} Y_s C_{p_s} \quad \text{and} \quad C_{v_{mixt}} = \sum_{s=1}^{ns} Y_s C_{v_s}; \quad (21)$$

Table 2 : Molecular weight of the chemical species.

Species	Molecular Weight (g/g-mol)
N	14.008
N ₂	28.016
NO	30.008
O	16.000
O ₂	32.000

Therefore, the mixture frozen ratio of specific heats, γ_f, is defined by:

$$\gamma_f = C_{p_{mixt}} / C_{v_{mixt}}. \quad (22)$$

The mixture translational/rotational temperature is obtained from Eq. (13), in the two-dimensional case:

$$T = \left[e/\rho - \sum_{s=1}^{ns} Y_s h_s^0 - 1/2(u^2 + v^2) \right] / \left(\sum_{s=1}^{ns} Y_s C_{v_s} \right) \quad (23)$$

and the mixture pressure is obtained from the Dalton law of the partial pressures:

$$p = \sum_{s=1}^{ns} \rho_s R_s T. \quad (24)$$

2.3 Transport model / Transport physical properties

The transport properties of a gaseous mixture are obtained by the [12] mixture general rule.

2.3.1 Mixture molecular viscosity

$$\mu = \sum_{s=1}^{ns} \frac{\mu_s}{\left[1 + \sum_{r \neq s} \frac{X_r}{X_s} \times \frac{M_s}{(M_s + M_r)} \left(\frac{5}{3} \times \frac{1}{A_{sr}^*} + \frac{M_r}{M_s} \right) \right] \phi_{sr}}, \quad (25)$$

in which:

μ_s is the molecular viscosity of the “s” specie, in kg/(m.s);

$$\phi_{sr} = \left[\frac{M_s}{8(M_s + M_r)} \right]^{-0.5} \left\{ F_{sr} + \left[\frac{\mu_s}{\mu_r} \times \left(\frac{M_r}{M_s} \right)^{0.5} \right]^{-0.5} B_{sr} \right\}^2; \quad (26)$$

$$A_{sr}^* = 5/3, B_{sr} = 1.0, F_{sr} = 1.0;$$

$$\frac{X_r}{X_s} = \left(\frac{\rho_r}{\rho} \times \frac{M}{M_r} \right) \times \left(\frac{\rho}{\rho_s} \times \frac{M_s}{M} \right) = \frac{\rho_r}{\rho_s} \times \frac{M_s}{M_r}. \quad (27)$$

Species molecular viscosity

According to [9], the species molecular viscosity can be determined by:

$$\mu_s = e^{E_{\mu s}} T^{[A_{\mu s}(\ln T)^3 + B_{\mu s}(\ln T)^2 + C_{\mu s} \ln T + D_{\mu s}]}, \text{ in g/(cm.s)}, \quad (28)$$

where: $A_{\mu s}, B_{\mu s}, C_{\mu s}, D_{\mu s}$ and $E_{\mu s}$ are constants defined in Table 3, valid to the interval 1,000 K $\leq T \leq 30,000$ K. To values below 1,000 K, it was employed the empiric formula of Sutherland to the air, applied to all species ([13]):

$$\mu_s = 1.458 \times 10^{-6} T^{1.5} / (T + 110.4), \text{ in kg/(m.s)}. \quad (29)$$

Table 3 : Coefficients $A_{\mu s}, B_{\mu s}, C_{\mu s}, D_{\mu s}$ and $E_{\mu s}$ to N, N₂, NO, O and O₂.

S ⁽¹⁾	A _{μs}	B _{μs}	C _{μs}	D _{μs}	E _{μs}
N	0.0	0.0	0.0120	0.5930	-12.3805
N ₂	0.0	0.0	0.0203	0.4329	-11.8153
NO	0.0	0.0	0.0452	-0.0609	-9.4596
O	0.0	0.0	0.0205	0.4257	-11.5803
O ₂	0.0	0.0	0.0484	-0.1455	-8.9231

⁽¹⁾ S = Species.

2.3.2 Mixture thermal conductivity

It is defined by the same formula of the molecular viscosity, replacing μ by k ; in other words:

$$k = \sum_{s=1}^{ns} \left[\frac{k_s}{1 + \sum_{r \neq s} \frac{X_r}{X_s} \times \frac{M_s}{(M_s + M_r)} \left(\frac{5}{3} \times \frac{1}{A_{sr}^*} + \frac{M_r}{M_s} \right)} \right] \phi_{sr}, \quad (30)$$

where:

k_s is the thermal conductivity of the “s” species, in J/(m.s.K);

$$\phi_{sr} = \left[\frac{M_s}{8(M_s + M_r)} \right]^{-0.5} \left\{ F_{sr} + \left[\frac{k_s}{k_r} \times \left(\frac{M_r}{M_s} \right)^{0.5} \right]^{-0.5} B_{sr} \right\}^2$$

and the other parameters defined according to Eq. (27).

Species frozen thermal conductivity

According to [14], the species frozen thermal conductivity can be determined by:

$$k_s = e^{E_{k f, s}} T^{[A_{k f, s}(\ln T)^3 + B_{k f, s}(\ln T)^2 + C_{k f, s} \ln T + D_{k f, s}]}, \quad (31)$$

in cal/(cm.s.K),

where: $A_{k f, s}, B_{k f, s}, C_{k f, s}, D_{k f, s}$ and $E_{k f, s}$ are constants defined in Table 4, valid to the interval 1,000 K $\leq T \leq 30,000$ K. To values below 1,000 K, it was employed the empiric formula of Sutherland to the air, applied to all species ([13]):

$$k_s = 2.495 \times 10^{-3} T^{1.5} / (T + 194.0), \text{ in J/(m.s.K)}. \quad (32)$$

Table 4 : Coefficients $A_{k f, s}, B_{k f, s}, C_{k f, s}, D_{k f, s}$ and $E_{k f, s}$ to N, N₂, NO, O and O₂.

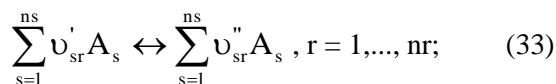
S ⁽¹⁾	A _{kf,s}	B _{kf,s}	C _{kf,s}	D _{kf,s}	E _{kf,s}
N	0.0	0.0	0.0169	0.5373	-12.8682
N ₂	0.0418	-1.2720	14.4571	-71.9660	122.5745
NO	0.0263	-0.8130	9.4203	-47.6841	79.4139
O	0.0	0.0	0.0319	0.2485	-11.6657
O ₂	0.0776	-2.5007	30.1390	-160.1758	307.3634

⁽¹⁾ S = Species.

2.4 Chemical model

2.4.1 Law of mass action

The symbolic representation of a reaction adopted in the present work follows the formulation of [1] and is given by:



and the law of mass action applied to this system of chemical reactions is defined by:

$$\dot{\omega}_s = M_s \sum_{r=1}^{nr} (\nu_{sr}'' - \nu_{sr}') \left\{ k_{fr} \prod_{s=1}^{ns} \left(\frac{\rho_s}{M_s} \right)^{\nu_{sr}'} - k_{br} \prod_{s=1}^{ns} \left(\frac{\rho_s}{M_s} \right)^{\nu_{sr}''} \right\}, \quad (34)$$

Table 5 : Chemical reactions and forward coefficients.

Reaction	Forward reaction rate coefficients, k_{fr} , $\text{cm}^3/(\text{mol.s})$	Third body
$\text{O}_2 + \text{M} \leftrightarrow 2\text{O} + \text{M}$	$3.61 \times 10^{18} T^{-1.0} e^{(-59,400/T)}$	O, N, O ₂ , N ₂ , NO
$\text{N}_2 + \text{M} \leftrightarrow 2\text{N} + \text{M}$	$1.92 \times 10^{17} T^{-0.5} e^{(-113,100/T)}$	O, O ₂ , N ₂ , NO
$\text{N}_2 + \text{N} \leftrightarrow 2\text{N} + \text{N}$	$4.15 \times 10^{22} T^{-0.5} e^{(-113,100/T)}$	-
$\text{NO} + \text{M} \leftrightarrow \text{N} + \text{O} + \text{M}$	$3.97 \times 10^{20} T^{-1.5} e^{(-75,600/T)}$	O, N, O ₂ , N ₂ , NO
$\text{NO} + \text{O} \leftrightarrow \text{O}_2 + \text{N}$	$3.18 \times 10^9 T^{1.0} e^{(-19,700/T)}$	-
$\text{N}_2 + \text{O} \leftrightarrow \text{NO} + \text{N}$	$6.75 \times 10^{13} e^{(-37,500/T)}$	-

in which: A_s represents the chemical symbol of the “s” species; “ns” is the number of studied chemical

species (reactants and products) involved in the considered reaction; “nr” is the number of reactions considered in the chemical model; ν_{sr}' and ν_{sr}'' are the Stoichiometric coefficients to reactants and products, respectively; and $k_{fr} = AT^B e^{-C/T}$ and $k_{br} = DT^{-E}$, with A, B, C, D and E being constants of the specific chemical reaction under study (“fr” = forward reaction and “br” = backward reaction). In the present work, ns = 5 and nr = 17. Tables 5 and 6 present the values of A, B, C, D and E to the seventeen (17) chemical reactions to be studied, in the forward and backward senses, respectively.

Table 6 : Chemical reactions and backward coefficients.

Reaction	Backward reaction rate coefficients, k_{br} , $\text{cm}^3/(\text{mol.s})$ or $\text{cm}^6/(\text{mol}^2.\text{s})$	Third body
$\text{O}_2 + \text{M} \leftrightarrow 2\text{O} + \text{M}$	$3.01 \times 10^{15} T^{-0.5}$	O, N, O ₂ , N ₂ , NO
$\text{N}_2 + \text{M} \leftrightarrow 2\text{N} + \text{M}$	$1.09 \times 10^{16} T^{-0.5}$	O, O ₂ , N ₂ , NO
$\text{N}_2 + \text{N} \leftrightarrow 2\text{N} + \text{N}$	$2.32 \times 10^{21} T^{-0.5}$	-
$\text{NO} + \text{M} \leftrightarrow \text{N} + \text{O} + \text{M}$	$1.01 \times 10^{20} T^{-1.5}$	O, N, O ₂ , N ₂ , NO
$\text{NO} + \text{O} \leftrightarrow \text{O}_2 + \text{N}$	$9.63 \times 10^{11} T^{0.5} e^{(-3,600/T)}$	-
$\text{N}_2 + \text{O} \leftrightarrow \text{NO} + \text{N}$	1.5×10^{13}	-

2.4.2 Air chemical model

In the present work, five (5) chemical species (N, N₂, NO, O and O₂) and seventeen (17) chemical

reactions [dissociation of N_2 and O_2 , formation of N , NO and O , and shuffle or exchange reactions (recombination reactions)] were studied. The reactions are as follows:

(a) Reactions of dissociation due to impact:

- (1) $O_2+O_2\leftrightarrow 2O+O_2$;
- (2) $N_2+O_2\leftrightarrow 2N+O_2$;
- (3) $NO+O_2\leftrightarrow N+O+O_2$;
- (4) $O_2+O\leftrightarrow 2O+O$;
- (5) $N_2+O\leftrightarrow 2N+O$;
- (6) $NO+O\leftrightarrow N+O+O$;
- (7) $O_2+N\leftrightarrow 2O+N$;
- (8) $N_2+N\leftrightarrow 2N+N$;
- (9) $NO+N\leftrightarrow N+O+N$.
- (10) $O_2+NO\leftrightarrow 2O+NO$;
- (11) $N_2+NO\leftrightarrow 2N+NO$;
- (12) $NO+NO\leftrightarrow N+O+NO$;
- (13) $O_2+N_2\leftrightarrow 2O+N_2$;
- (14) $N_2+N_2\leftrightarrow 2N+N_2$;
- (15) $NO+N_2\leftrightarrow N+O+N_2$;

(b) Reactions of shuffle or exchange:

- (16) $NO+O\leftrightarrow O_2+N$;
- (17) $N_2+O\leftrightarrow NO+N$.

The Stoichiometric coefficients of these reactions for each species are presented in [10].

3 Structured Algorithm of [6] in Two-Dimensions

The numerical procedure to the solution of the convective flux consists in uncouple the Euler equations in two parts, according to [15]. One convective part associated with the dynamic flux of the reactive Euler equations and the other convective part associated with the chemical flux of the reactive Euler equations. The separation is described as follows.

The approximation to the integral equation (1) to a rectangular finite volume yields a system of ordinary differential equations with respect to time defined by:

$$V_{i,j} \frac{dQ_{i,j}}{dt} = -R_{i,j}, \quad (35)$$

with $R_{i,j}$ representing the net flux (residual) of mass conservation, general and of species, of the linear momentum conservation and of total energy in the volume $V_{i,j}$. One graphic representation of the

rectangular computational cell of volume $V_{i,j}$, with its nodes and respective flux interfaces, is presented in Fig. 1. The volume $V_{i,j}$ of the computational cell described above is determined by:

$$V_{i,j} = 0.5 \left[(x_{i,j} - x_{i+1,j})y_{i+1,j+1} + (x_{i+1,j} - x_{i+1,j+1})y_{i,j} + (x_{i+1,j+1} - x_{i,j})y_{i+1,j} \right] + 0.5 \left[(x_{i,j} - x_{i+1,j+1})y_{i,j+1} + (x_{i+1,j+1} - x_{i,j+1})y_{i,j} + (x_{i,j+1} - x_{i,j})y_{i+1,j+1} \right]. \quad (36)$$

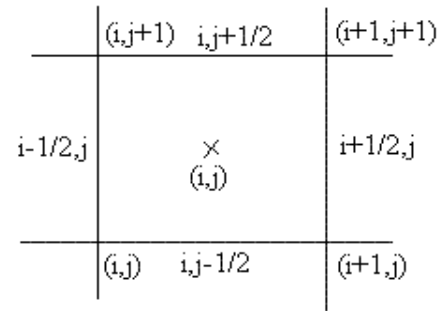


Figure 1 : Structured Computational Cell, Nodes and Flux Interfaces.

The components of the unity vector normal to the flux interface and the area of the flux interface “ l ”, n_x^l , n_y^l and S^l , are defined as:

$$\begin{aligned} n_x^l &= \Delta y_1 / (\Delta x_1^2 + \Delta y_1^2)^{0.5}, \\ n_y^l &= -\Delta x_1 / (\Delta x_1^2 + \Delta y_1^2)^{0.5} \\ S^l &= (\Delta x_1^2 + \Delta y_1^2)^{0.5}. \end{aligned} \quad (37)$$

Expressions to Δx_1 and Δy_1 are given in Table 7.

Table 7 : Values of Δx_1 and Δy_1 to the structured case.

Interface	Δx_1	Δy_1
$l = (i,j-1/2)$	$x_{i+1,j} - x_{i,j}$	$y_{i+1,j} - y_{i,j}$
$l = (i+1/2,j)$	$x_{i+1,j+1} - x_{i+1,j}$	$y_{i+1,j+1} - y_{i+1,j}$
$l = (i,j+1/2)$	$x_{i,j+1} - x_{i+1,j+1}$	$y_{i,j+1} - y_{i+1,j+1}$
$l = (i-1/2,j)$	$x_{i,j} - x_{i,j+1}$	$y_{i,j} - y_{i,j+1}$

The residual is calculated as:

$$R_{i,j} = R_{i,j-1/2} + R_{i+1/2,j} + R_{i,j+1/2} + R_{i-1/2,j}, \quad (38)$$

where $R_{i+1/2,j} = R_{i+1/2,j}^e - R_{i+1/2,j}^v$, with “e” representing the residual associated with the flux of the Euler equations and “v” representing the residual associated with the viscous flux. The residuals are summed because the area components are considered with their respective coordinate signals.

The discrete flux of the Euler equations or the discrete convective flux calculated in this work follows the procedure described by the AUSM scheme (Advection Upstream Splitting Method) of [16]. This flux can be interpreted as a sum involving the arithmetical average between the right (R) and the left (L) states of the (i+1/2,j) cell face, related to cells (i,j) and (i+1,j), respectively, multiplied by the interface Mach number, and a scalar dissipative term, as shown in [16]. Hence, the discrete-dynamic-convective-flux vector is defined by:

$$R_{i+1/2,j} = |S_{i+1/2,j}| \left\{ \frac{1}{2} M_{i+1/2,j} \left[\begin{array}{c} (\rho a) \\ \rho a u \\ \rho a v \\ (\rho a H)_L \end{array} \right] + \begin{array}{c} (\rho a) \\ \rho a u \\ \rho a v \\ (\rho a H)_R \end{array} \right\} - \frac{1}{2} \phi_{i+1/2,j} \left[\begin{array}{c} (\rho a) \\ \rho a u \\ \rho a v \\ (\rho a H)_R \end{array} \right] - \begin{array}{c} (\rho a) \\ \rho a u \\ \rho a v \\ (\rho a H)_L \end{array} \right\} + \begin{array}{c} 0 \\ S_x p \\ S_y p \\ 0 \end{array} \Bigg|_{i+1/2,j} \quad (39)$$

and the discrete-chemical-convective-flux vector is defined by:

$$R_{i+1/2,j} = |S_{i+1/2,j}| \left\{ \frac{1}{2} M_{i+1/2,j} \left[\begin{array}{c} (\rho_1 a) \\ \rho_2 a \\ \rho_3 a \\ (\rho_4 a)_L \end{array} \right] + \begin{array}{c} (\rho_1 a) \\ \rho_2 a \\ \rho_3 a \\ (\rho_4 a)_R \end{array} \right\} - \frac{1}{2} \phi_{i+1/2,j} \left[\begin{array}{c} (\rho_1 a) \\ \rho_2 a \\ \rho_3 a \\ (\rho_4 a)_R \end{array} \right] - \begin{array}{c} (\rho_1 a) \\ \rho_2 a \\ \rho_3 a \\ (\rho_4 a)_L \end{array} \right\}, \quad (40)$$

where $S_{i+1/2,j} = [S_x \ S_y]^T$ defines the normal area vector to the flux interface (i+1/2,j), in which the area components are defined by:

$$S_x^{i+1/2,j} = n_x^{i+1/2,j} (S^{i+1/2,j}),$$

$$S_y^{i+1/2,j} = n_y^{i+1/2,j} (S^{i+1/2,j}). \quad (41)$$

The quantity “a” represents the sound speed, calculated as:

$$a = \sqrt{\gamma_f p / \rho}, \quad (42)$$

to a thermal equilibrium formulation. $M_{i+1/2,j}$ defines the advective Mach number at the face (i+1/2,j) of cell (i,j), which is calculated according to [16] as:

$$M_{i+1/2,j} = M_L^+ + M_R^-, \quad (43)$$

where the separated Mach numbers, $M^{+/-}$, are defined by [6] as:

$$M^+ = \begin{cases} M, & \text{if } M \geq 1; \\ 0.25(M+1)^2, & \text{if } |M| < 1; \\ 0, & \text{if } M \leq -1; \end{cases}$$

$$M^- = \begin{cases} 0, & \text{if } M \geq 1; \\ -0.25(M-1)^2, & \text{if } |M| < 1; \\ M, & \text{if } M \leq -1. \end{cases} \quad (44)$$

M_L and M_R represent the Mach numbers associated with the left and right states, respectively. The advection Mach number is defined as:

$$M = (S_x u + S_y v) / (a |S|). \quad (45)$$

The pressure at face (i+1/2,j) of cell (i,j) is calculated in a similar way:

$$p_{i+1/2,j} = p_L^+ + p_R^-, \quad (46)$$

with $p^{+/-}$ representing the pressure separation defined according to [6]:

$$p^+ = \begin{cases} p, & \text{if } M \geq 1; \\ 0.25p(M+1)^2(2-M), & \text{if } |M| < 1; \\ 0, & \text{if } M \leq -1; \end{cases}$$

$$p^- = \begin{cases} 0, & \text{if } M \geq 1; \\ 0.25p(M-1)^2(2+M), & \text{if } |M| < 1; \\ p, & \text{if } M \leq -1. \end{cases} \quad (47)$$

The definition of the dissipation term ϕ determines the particular formulation of the convective fluxes. The choice below corresponds to the [6] scheme, according to [17]:

$$\phi_{i+1/2,j} = \phi_{i+1/2,j}^{VL} = \begin{cases} |M_{i+1/2,j}|, & \text{if } |M_{i+1/2,j}| \geq 1; \\ |M_{i+1/2,j}| + 0.5(M_R - 1)^2, & \text{if } 0 \leq M_{i+1/2,j} < 1; \\ |M_{i+1/2,j}| + 0.5(M_L + 1)^2, & \text{if } -1 < M_{i+1/2,j} \leq 0. \end{cases} \quad (48)$$

The time integration is performed employing a Runge-Kutta explicit method of five stages, second-order accurate, to the two types of convective flux. To the dynamic part, this method can be represented in general form as:

$$\begin{aligned} Q_{i,j}^{(0)} &= Q_{i,j}^{(n)} \\ Q_{i,j}^{(k)} &= Q_{i,j}^{(0)} - \alpha_k \Delta t_{i,j} R(Q_{i,j}^{(k-1)}) / V_{i,j}, \quad (49) \\ Q_{i,j}^{(n+1)} &= Q_{i,j}^{(k)} \end{aligned}$$

and to the chemical part it can be represented in general form by:

$$\begin{aligned} Q_{i,j}^{(0)} &= Q_{i,j}^{(n)} \\ Q_{i,j}^{(k)} &= Q_{i,j}^{(0)} - \alpha_k \Delta t_{i,j} [R(Q_{i,j}^{(k-1)}) / V_{i,j} - S_C(Q_{i,j}^{(k-1)})], \quad (50) \\ Q_{i,j}^{(n+1)} &= Q_{i,j}^{(k)} \end{aligned}$$

where $k = 1, \dots, 5$; $\alpha_1 = 1/4$, $\alpha_2 = 1/6$, $\alpha_3 = 3/8$, $\alpha_4 = 1/2$ and $\alpha_5 = 1$. This scheme is first-order accurate in space and second-order accurate in time. The second-order of spatial accuracy is obtained by the MUSCL procedure (details in [7]).

The [6] scheme in its first-order two-dimensional unstructured version to an ideal gas formulation is presented in [18]. The extension to reactive flow in thermal equilibrium and chemical non-equilibrium can be deduced from the present code. This task will be done in a next paper to be published by the authors, which describes the unstructured algorithm to thermal equilibrium and chemical non-equilibrium in two-dimensions.

The viscous formulation follows that of [19], which adopts the Green theorem to calculate primitive variable gradients. The viscous vectors are obtained by arithmetical average of flow properties between cell (i,j) and its neighbors. As was done with the convective terms, there is a need to separate the viscous flux in two parts: dynamical viscous flux and chemical viscous flux. The dynamical part corresponds to the first four equations of the Navier-Stokes ones and the chemical part corresponds to the last four equations.

A spatially variable time step procedure was employed aiming to accelerate the convergence of the numerical schemes. This technique has provided excellent convergence gains as demonstrated in [4-5] and is implemented in the present codes.

4 Results

Tests were performed in three microcomputers. Four (4) orders of reduction of the maximum residual were adopted as convergence criterion. In the simulations, the attack angle was set equal to zero.

4.1 Initial and boundary conditions to the studied problem

The initial conditions are presented in Table 8. The Reynolds number is obtained from data of [20]. The boundary conditions to this problem of reactive flow are detailed in [10], as well the geometry in study, the meshes employed in the simulations and the description of the computational configuration. The geometry is a blunt body with 1.0 m of nose ratio and parallel rectilinear walls. The far field is located at 20.0 times the nose ratio in relation to the configuration nose. The dimensionless employed in the Euler and Navier-Stokes equations in this study are also described in [10].

Table 8 : Initial conditions to the problem of the blunt body.

Property	Value
M_∞	8.78
ρ_∞	0.00326 kg/m ³
p_∞	687.0 Pa
U_∞	4,776 m/s
T_∞	694.0 K
Altitude	40,000 m
Y_N	10 ⁻⁹
Y_{N_2}	0.73555
Y_{NO}	0.05090
Y_O	0.07955
L	2.0 m
Re_∞	2.3885x10 ⁶

4.2 Studied cases

Table 9 presents the studied cases in this work, the mesh characteristics and the order of accuracy of the [6] scheme.

Table 9 : Studied cases, mesh characteristics and accuracy order.

Case	Mesh	Accuracy order
Inviscid – 2D	63x60	First ^a
Viscous – 2D	63x60 (7.5%) ^c	First ^a
Inviscid – 2D	63x60	Second ^a
Viscous – 2D	63x60 (7.5%)	Second ^a
Inviscid – 2D	63x60	First ^b
Viscous – 2D	53x60 (5.0%)	First ^b

^a Structured spatial discretization; ^b Unstructured spatial discretization; ^c Exponential stretching.

4.3 Results in thermal equilibrium and chemical non-equilibrium

4.3.1 Inviscid, structured and first-order accurate case

Figure 2 presents the pressure contours in the field. The pressure peak is at the configuration nose, as expected. The solution presents good symmetry properties. There are not pre- or post-shock oscillations.

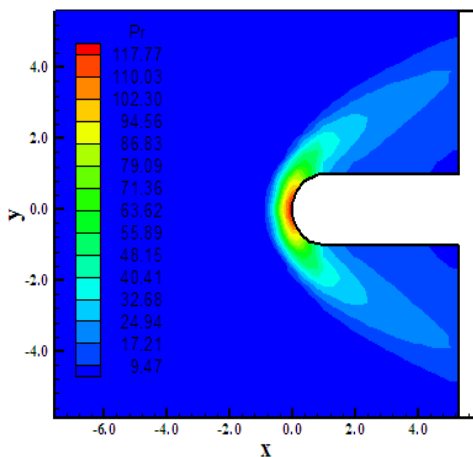


Figure 2 : Pressure Contours.

Figure 3 exhibit the Mach number contours. Good symmetry properties are again observed in the solution and the shock is well captured. The flow is slowdown due to the presence of the configuration and in the line of stagnation, behind the shock, the flow is subsonic.

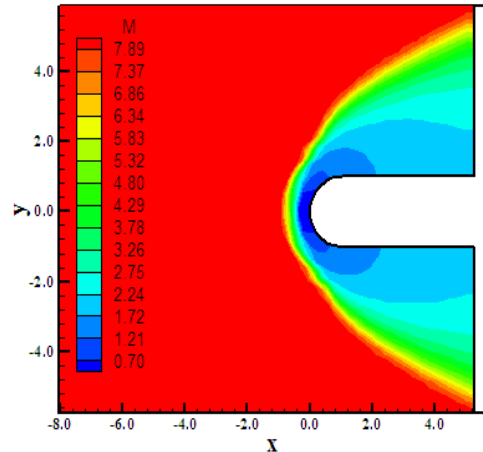


Figure 3 : Mach Number Contours.

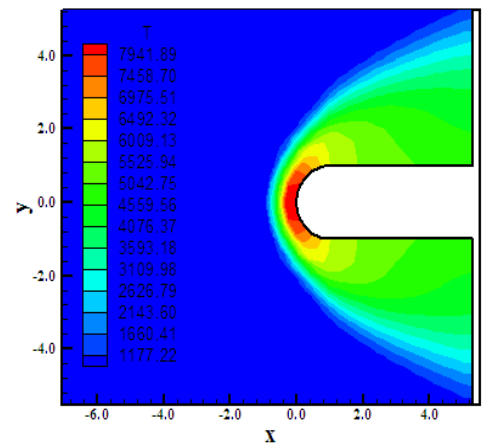


Figure 4 : T/R Temperature Contours.

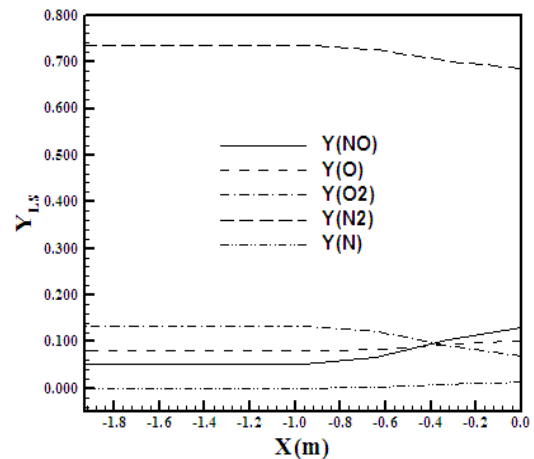


Figure 5 : Mass Fraction Distribution at the Line of Stagnation.

Figure 4 shows the translational/rotational-temperature-field contours. The temperature peak reaches 7,940 K, what represents that in this region exists the O_2 and N_2 dissociation. This region, in the inviscid case, is restricted to the region of the configuration nose. The shock wave is well captured and the contours present good symmetry characteristics. Figure 5 exhibits the mass fraction distribution of the five studied chemical species: N, N_2 , NO, O and O_2 , along the configuration line of stagnation. It is notable enough the dissociation of the N_2 and of the O_2 , with the consequent formation of NO, O and N. The formation of the NO behind the shock, particularly, is more meaningful than the others due to the fact of the dissociation of O_2 and the considerable dissociation of N_2 .

4.3.2 Viscous, structured and first-order accurate case

Figure 6 presents the pressure contours. Good symmetry characteristics are observed. The viscous pressure field is more severe than the one due to the inviscid case, because of, mainly, to the transport phenomena associated to the viscosity, which are considered.

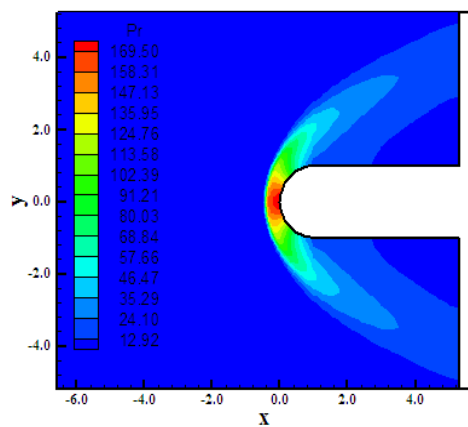


Figure 6 : Pressure Contours.

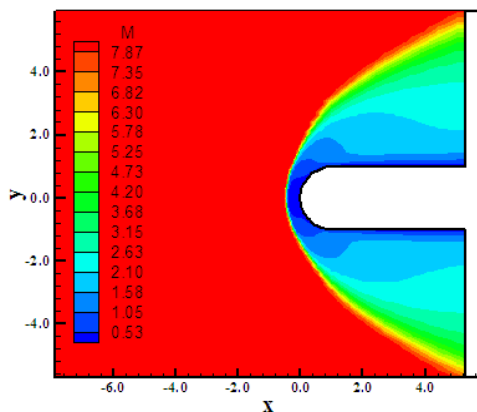


Figure 7 : Mach Number Contours.

Figure 7 exhibits the Mach number contours obtained from the simulation. Good symmetry is observed. The region of low Mach number along the blunt body demonstrates that the adherence and impermeability conditions were guaranteed.

Figure 8 shows the translational/rotational temperature contours to the viscous case. As can be observed, the temperature peak exceeds 8,700 K close to the geometry, what represent the dissociation of O_2 and N_2 in this region. This was the expected behavior since the physical transport phenomena of viscosity and thermal conductivity were considered, taking into account adiabatic wall. Good symmetry characteristics are observed. Figure 9 presents the mass fraction distribution from the five chemical species studied in this work: N, N_2 , NO, O and O_2 , along the line of stagnation of the blunt body geometry. It is possible to observe, in relation to the inviscid case, bigger dissociation of N_2 and O_2 close to the wall and a slight increase in the formation of NO. The N also has an increase in its formation in relation to the inviscid case.

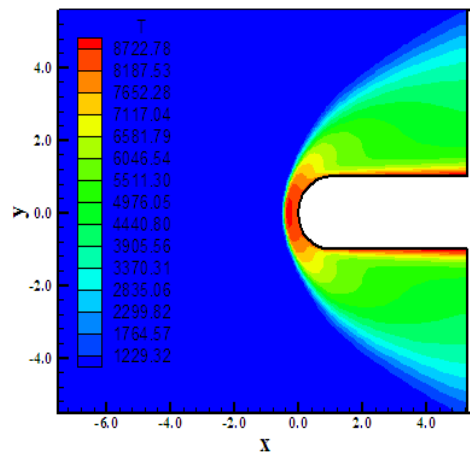


Figure 8 : T/R Temperature Contours.

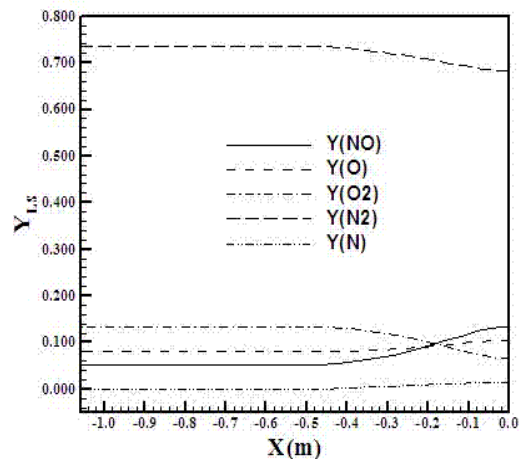


Figure 9 : Mass Fraction Distribution at the Line of Stagnation.

4.3.3 Inviscid, structured and second-order accurate case

Figure 10 exhibits the pressure contours to the problem of the blunt body, employing the [6] scheme using the MUSCL procedure to obtain second-order accuracy. This MUSCL procedure employs a non-linear flux limiter type “minmod”. The solution presents good characteristics of symmetry. In quantitative terms, this pressure field is more severe than the one due to the first-order solution. Figure 11 shows the Mach number contours to this problem of the blunt body submitted to an inviscid flow. Good symmetry characteristics are observed. Behind the normal shock, the flow becomes subsonic because of the intensity of this one.

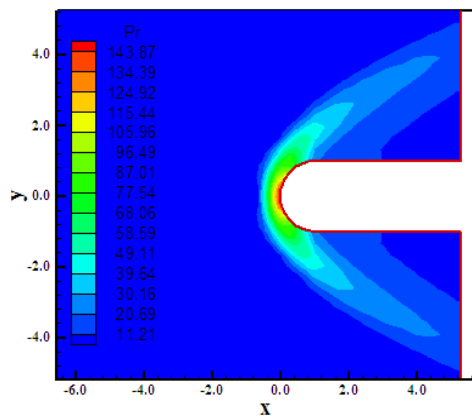


Figure 10 : Pressure Contours.

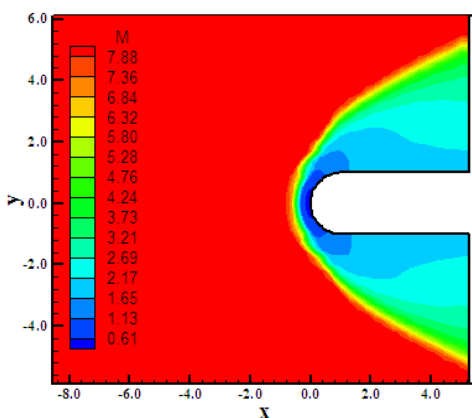


Figure 11 : Mach Number Contours.

Figure 12 exhibits the translational / rotational temperature distribution in the computational domain. As can be perceived, the temperature field to this simulation of second-order is also more intense than the one due to the first-order solution. The temperature peak is superior to 8,100 K at the configuration nose, what express a bigger dissociation of O_2 and N_2 in this region. It is also

possible to observe that due to the not formulation of transport mechanisms, like viscosity, thermal conductivity and species diffusion (Fick law), the temperature peak stays confined to the configuration-nose region, does not propagating along the blunt body, as expected to a inviscid formulation. Figure 13 presents the mass fraction distribution of the five researched-chemical species in this work along the line of stagnation of the blunt body. As can be observed, there is minor dissociation of N_2 and O_2 along the line of stagnation than the one due to the first-order solution. The formation of N is also discrete as compared with the others and with the first-order solution. The formation of NO and O are also inferior to those obtained with the first-order solution.

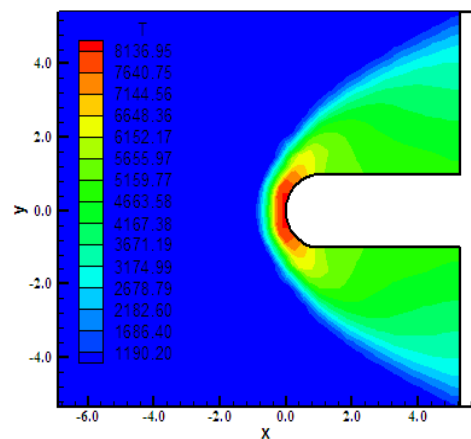


Figure 12 : T/R Temperature Contours.

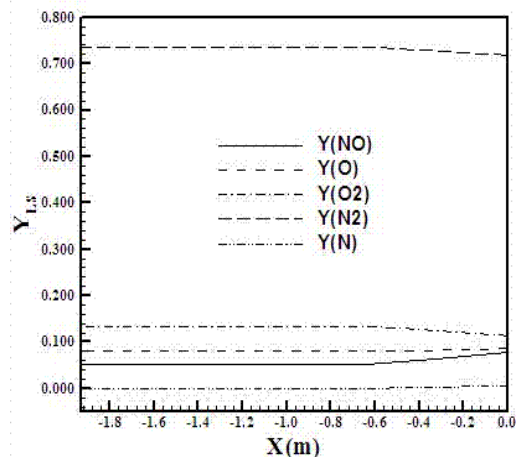


Figure 13 : Mass Fraction Distribution at the Line of Stagnation.

It is important to emphasize that, although the first-order solution estimates bigger formations of NO and N at the line of stagnation and bigger

dissociations of N_2 and O_2 also at the line of stagnation, this occurs exactly at the line of stagnation. The contours of the mass fraction detect an increase in the formation of the N and of the NO along the blunt body, opposed to the observed at the line of stagnation. It is true because both regions are different: line of stagnation and blunt body. Hence, to the more precise solution, the second-order solution, there was a reduction in the dissociation of the N_2 and O_2 at the line of stagnation and along the blunt body, reduction of the formation of the N and NO at the line of stagnation and increase of the N, NO and O along the blunt body.

4.3.4 Viscous, structured and second-order accurate case

Figure 14 shows the pressure contours to the problem of the blunt body, in two-dimensions, considering viscous flow simulated with the [6] scheme of second-order TVD (Total Variation Diminishing). The pressure peak is lower than the respective one due to the first-order solution. The pressure field is in general less severe than the respective one due to the first-order solution.

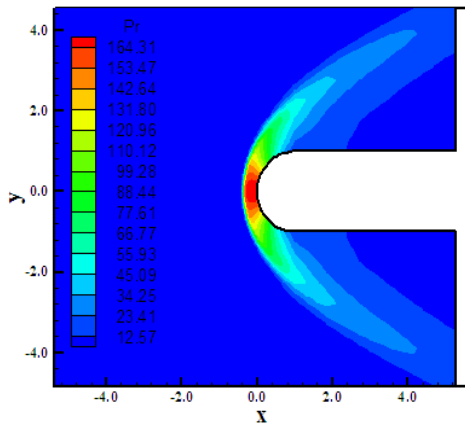


Figure 14 : Pressure Contours.

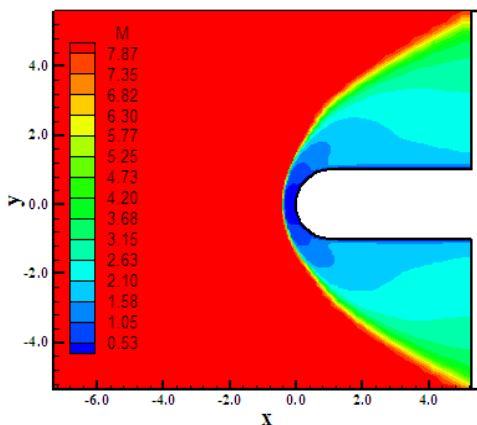


Figure 15: Mach Number Contours.

The Mach number contours are exhibited in Fig. 15. They present good symmetry characteristics and the shock wave is closer than the inviscid solution due to the employed mesh stretching and due to the reactive effects of the viscous simulation. As can also be observed, the region of low velocity propagates along the blunt body, satisfying the conditions of adherence and impermeability of the viscous formulation.

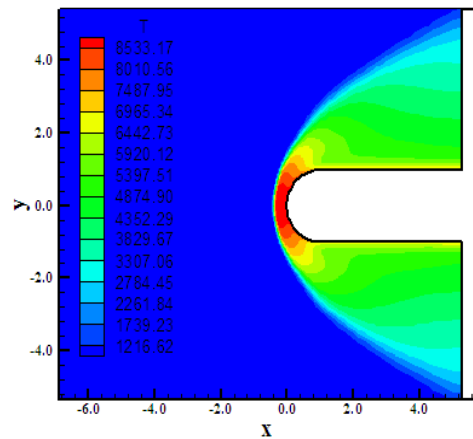


Figure 16 : T/R Temperature Contours.

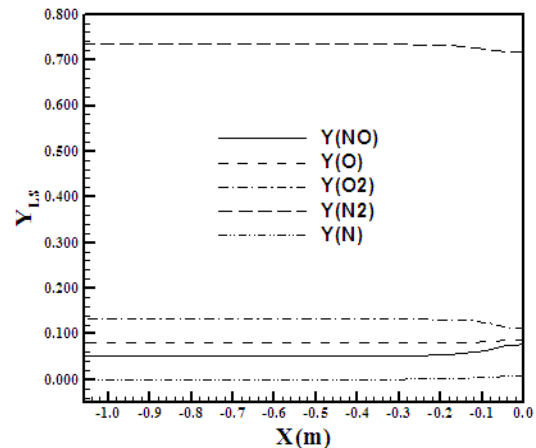


Figure 17 : Mass Fraction Distribution at the Line of Stagnation.

Figure 16 presents the translational/rotational temperature distribution in the computational domain. The translational/rotational temperature peak, approximately 8,500 K, was inferior to the respective peak obtained by the first-order solution. The influence of the translational/rotational temperature is confined to a very much restrict region, which corresponds to the boundary layer, due to the consideration of the transport phenomena (viscosity, thermal conductivity and species diffusion). Figure 17 exhibits the mass fraction distribution of the five chemical species studied in

this work, namely: N, N₂, NO, O and O₂, along the line of stagnation of the blunt body. As can be observed, an increase in the formation of the NO, of O and of the N, with the respective reduction in the N₂ and O₂ species due to dissociation, occurs. The physical phenomena expected to be observed occurred in this second-order solution. With this, it is possible to conclude that the second-order solution present meaningful values of formation of N, NO and O, as well values of the reduction of the species N₂ and O₂, although more modest than those presented by the first-order-structured solution. This thinking does not want to say that the first-order solution is the correct one. Only it presented more dissociation of O₂ and N₂. The second-order solution present a different behaviour, more discrete in the dissociation of O₂ and N₂, resulting also in more discrete additions of N, NO and O. Due to this solution is of second-order, it should be considered as the most correct in its results.

4.3.5 Inviscid, unstructured and first-order accurate case

Figure 18 exhibits the pressure contours around the blunt body in the computational domain. This solution was obtained according to an unstructured-spatial-discretization context and, therefore, symmetry properties, in general, are not observed. The pressure field is more severe than that obtained with the respective structured first-order solution. Figure 19 shows the Mach number contours in the computational domain. A region of subsonic flow is formed at the configuration nose due to the shock wave in this region be normal. The shock contours present the expected behavior: normal shock at the blunt body nose, being attenuated until reach a Mach wave configuration, far from the geometry. This Mach wave is obtained through successive oblique shock waves acting over the normal shock.

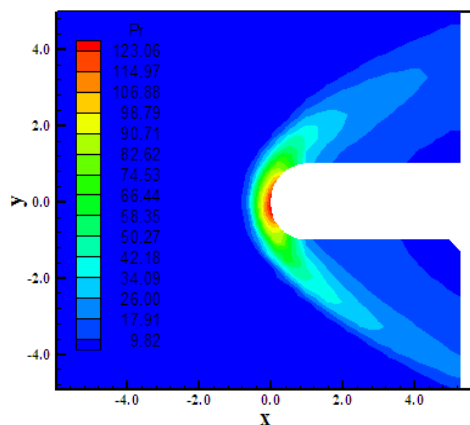


Figure 18 : Pressure Contours.

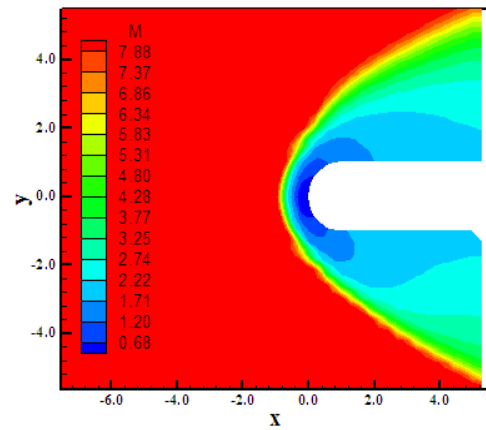


Figure 19 : Mach Number Contours.

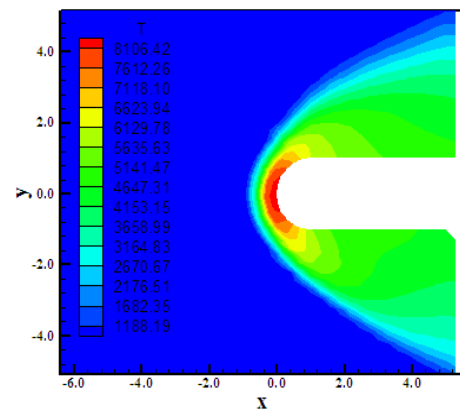


Figure 20 : T/R Temperature Contours.

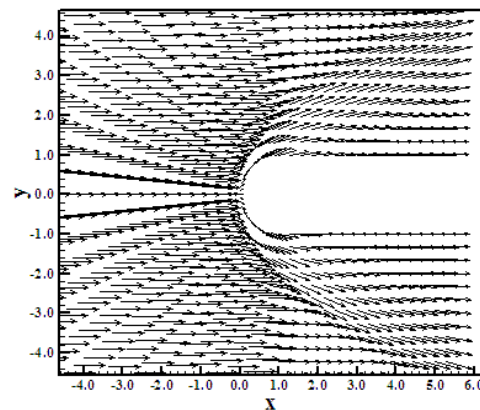


Figure 21 : Velocity Vector Field.

Figure 20 exhibits the temperature distribution in the computational domain of the simulation. The temperature peak, superior to 8,100 K at the geometry nose, is bigger than the respective temperature peak of the structured-first-order solution. It is expected, with this value of temperature, dissociation of O₂ and of N₂ in this region. With this analysis, it has considerable increase in the mass fractions of N, NO and O.

Figure 21 shows the velocity vector field, assuring that the tangency condition is satisfied by the adopted inviscid formulation.

4.3.6 Viscous, unstructured and first-order accurate case

Figure 22 presents the pressure contours obtained in the computational domain to the unstructured and viscous case. This pressure field is less severe than the one obtained by the structured-first-order solution. This solution presents more symmetry than its inviscid contra part and presents the shock position closer to the configuration nose, as expected by a viscous and reactive solution. Figure 23 shows the Mach number contours. Behind the normal shock, a subsonic region is formed, as expected. This region is extended along the blunt body, at the lower and upper surfaces. Better characteristics of symmetry are observed because of the employment of a more refined mesh. The shock wave behaves as expected: normal at the blunt body nose and attenuated until reaches a Mach wave configuration, far from the geometry under study.

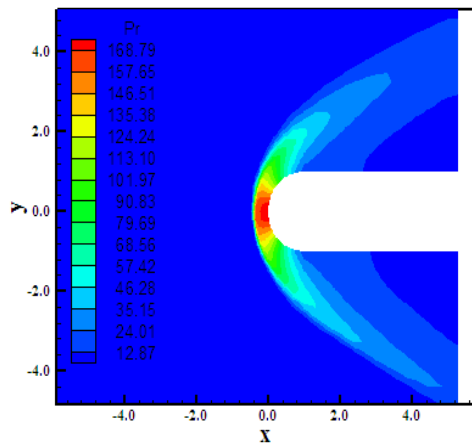


Figure 22 : Pressure Contours.

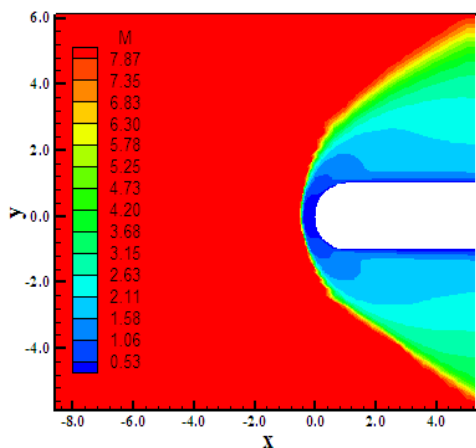


Figure 23 : Mach Number Contours.

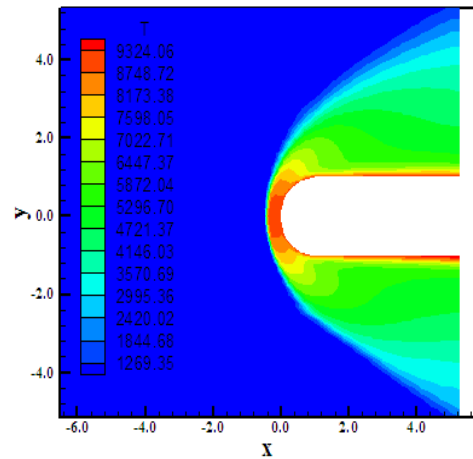


Figure 24 : T/R Temperature Contours.

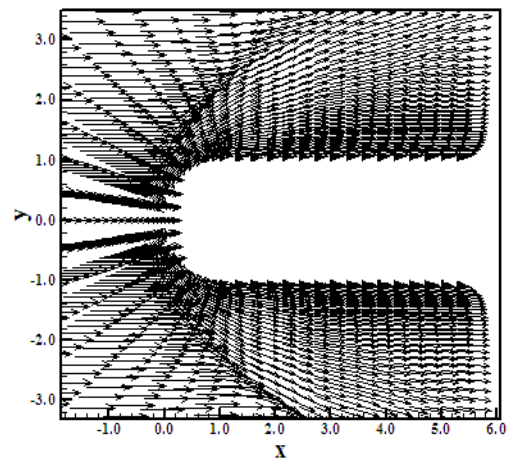


Figure 25 : Velocity Vector Field.

Figure 24 presents the contours of the distribution of the translational/rotational temperature in the calculation domain. The temperature peak reaches more than 9,300 K at the nose and along the blunt body walls. This implies that, in these regions, the O_2 and N_2 are dissociated, having bigger formation of N , NO and O than in the structured-viscous-first-order case. Figure 25 presents the velocity vector field to this viscous case. As observed, the adherence and impermeability conditions are satisfied by the employed viscous formulation.

4.3.7 Shock position

In this section is presented the behavior of the shock position in ideal and in thermal equilibrium and chemical non-equilibrium conditions. Only first-order solutions are compared because the second-order ideal gas solutions did not present converged ones.

The detached shock position in terms of pressure distribution, in the inviscid case and first-order accurate solution, is exhibited in Fig. 26. It is shown the ideal-gas-shock position and the thermal equilibrium and chemical non-equilibrium shock position. As can be observed, the ideal-gas-shock position is located at 1.25 m, whereas the thermal equilibrium and chemical non-equilibrium position is located at 0.90 m. As referred in the CFD literature, in reactive flow the shock is closer to the configuration. As can be observed in this inviscid solution, the reactive shock is actually closer to the blunt body than the ideal shock.

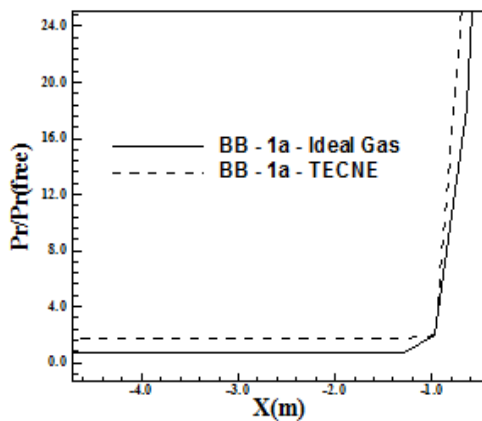


Figure 26 : Shock Detachment (Inviscid Case).

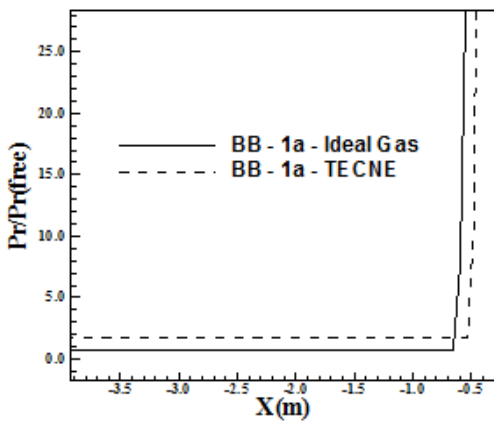


Figure 27 : Shock Detachment (Viscous Case).

The detached shock position in terms of pressure distribution, in the viscous case and first-order accurate solution, is exhibited in Fig. 27. It is shown the ideal-gas-shock position and the thermal equilibrium and chemical non-equilibrium shock position. As can be observed, the ideal-gas-shock position is located at 0.65 m, whereas the thermal equilibrium and chemical non-equilibrium position is located at 0.50 m. As mentioned above, in reactive flow the shock is closer to the

configuration. As can be observed in this viscous solution, the reactive shock is actually closer to the blunt body than the ideal shock.

4.3.8 Aerodynamic coefficients of lift and drag

Table 10 exhibits the aerodynamic coefficients of lift and drag obtained by the problem of the blunt body, with structured discretization, to the reactive formulation. These coefficients are due to the pressure term alone. The contribution of the friction term was not considered.

To the problem of the blunt body, a symmetric geometry in relation to the x axis, a zero value, or close to it, to the lift coefficient is expected. By Table 10, it is possible to note that the solution closest to this value to c_L was that of the [6] scheme with first-order accuracy, in an inviscid formulation. The maximum c_D was obtained by the solution of the [6] scheme, first-order accurate and employing a viscous formulation.

Table 10 : Aerodynamic coefficients of lift and drag to the structured blunt body case.

Studied Case	c_L	c_D
First-Order / Inviscid / TECNE ⁽¹⁾	-1.942×10^{-5}	0.952
First-Order/Viscous/TECNE	-6.225×10^{-5}	1.180
Second-Order / Inviscid / TECNE	-7.816×10^{-5}	1.055
Second-Order / Viscous / TECNE	-6.578×10^{-5}	1.134

⁽¹⁾ TECNE: Thermal Equilibrium and Chemical Non-Equilibrium.

4.4 Computational performance of the studied algorithms

Table 11 presents the computational data of the reactive simulations performed with the [6] scheme to the problem of the blunt body in two-dimensions. In this table are exhibited the studied case, the maximum number of CFL employed in the simulation, the number of iterations to convergence and the number of orders of reduction in the magnitude of the maximum residual in relation to its initial value to convergence. As can be observed, all test-cases converged with no minimal four orders of reduction in the value of the maximum residual. The maximum numbers of CFL presented the following distribution: 0.5 in two (2) cases (33.33%), 0.3 in

one (1) case (16.67%) and 0.1 in three (3) cases (50.00%). The convergence iterations did not overtake 7,800, in all studied cases. However, the time wasted in the simulations was much raised, taking until weeks to convergence (to four orders of reduction in the maximum residual and viscous case). This aspect can be verified in the computational costs presented in Table 12. It is important to emphasize that all two-dimensional viscous simulations were considered laminar, although high Reynolds number were employed in the simulations.

Table 11 : Computational data of the reactive simulations of the blunt body.

Studied Case	CFL	Iterations	Orders of Reduction of the Residual
First-Order/ Structured/ Inviscid/2D/ TECNE ⁽¹⁾	0.5	513	4
First-Order/ Structured/ Viscous/2D/ TECNE	0.5	1,450	4
Second-Order/ Structured/ Inviscid/2D/ TECNE	0.1	3,133	4
Second-Order/ Structured/ Viscous/2D/ TECNE	0.1	6,620	4
First-Order/ Unstructured /Inviscid/2D/ TECNE	0.3	1,312	4
First-Order/ Unstructured /Viscous/2D/ TECNE	0.1	7,747	4

⁽¹⁾ TECNE: Thermal Equilibrium and Chemical Non-Equilibrium.

Table 12 : Computational costs of the [6] scheme in the reactive cases.

Studied Case	Computational Cost ⁽¹⁾
Inviscid/First-Order/Structured/2D/TECNE	0.0008065
Viscous/First-Order/Structured /2D/TECNE	0.0011627
Inviscid/Second-Order/Structured /2D/TECNE	0.0009068
Viscous/Second-Order/Structured /2D/TECNE	0.0012641
Inviscid/First-Order/Unstructured /2D/TECNE	0.0007397
Viscous/First-Order/Unstructured /2D/TECNE	0.0010261

⁽¹⁾ Measured in seconds/per iteration/per computational cell.

Table 12 exhibits the computational costs of the [6] scheme in the two-dimensional reactive formulation. This cost is evaluated in seconds/per iteration/per computational cell. They were calculated using a notebook with 2.13 GHz of clock and 1.0 GBytes of RAM. In the two-dimensional case, considering thermal equilibrium and chemical non-equilibrium, the cheapest algorithm was due to [6], inviscid, first-order of accuracy, unstructured, although the most expensive was due to [6], viscous, second-order accurate, structured. In percentage terms, the former is 70.89% cheaper.

5 Conclusions

This work, the first part of this study, presents a numerical tool implemented to simulate inviscid and viscous flows employing the reactive gas formulation of thermal equilibrium and chemical non-equilibrium flow in two-dimensions. The Euler and Navier-Stokes equations, employing a finite

volume formulation, on the context of structured and unstructured spatial discretizations, are solved. These variants allow an effective comparison between the two types of spatial discretization aiming verify their potentialities: solution quality, convergence speed, computational cost, etc. The aerospace problem involving the “hot gas” hypersonic flow around a blunt body, in two-dimensions, is simulated.

To the simulations with unstructured spatial discretization, a structured mesh generator developed by the first authors ([21]), which create meshes of quadrilaterals (2D), was employed. After that, as a pre-processing stage ([22]), such meshes were transformed in meshes of triangles. Such procedure aimed to avoid the time which would be waste with the implementation of an unstructured generator, which was not the objective of the present work, and to obtain a generalized solver to the solution of the reactive equations.

In this work, first part of this study, the structured formulation of the two-dimensional Euler and Navier-Stokes reactive equations is presented. In a next paper, the second part of this study, it will be presented the unstructured version of the calculation algorithm in two-dimensions to complete the formulation in structured and in unstructured contexts.

The results have demonstrated that the most correct aerodynamic coefficient of lift is obtained by the [6] first-order accurate scheme in the inviscid, structured, blunt body simulation. The cheapest algorithm was the unstructured [6] scheme, first-order accurate in space, to an inviscid simulation. Moreover, the shock position is closer to the geometry as using the reactive formulation. It was verified in the inviscid and viscous cases.

In the [23] study, the results have demonstrated that the most critical pressure field was obtained by the [6] scheme, first-order accurate, viscous and in its structured version. Moreover, in this case, the peak temperature reached its maximum in this case. The cheapest algorithm was the [6] scheme, inviscid, first-order accurate and in its unstructured version. It was 115.51 % cheaper than the most expensive version of the [6] algorithm. The shock position determined by the thermal equilibrium and chemical non-equilibrium case was closer to the configuration nose than in the ideal gas case and in the respective two-dimensional case, ratifying the expected behavior highlighted in the CFD literature.

6 Acknowledgments

The first author acknowledges the CNPq by the financial support conceded under the form of a DTI (Industrial Technological Development) scholarship no. 384681/2011-5. He also acknowledges the infrastructure of the ITA that allowed the realization of this work.

References:

- [1] G. Degrez, and E. Van Der Weide, Upwind Residual Distribution Schemes for Chemical Non-Equilibrium Flows, *AIAA Paper 99-3366*, 1999.
- [2] M. Liu, and M. Vinokur, Upwind Algorithms for General Thermo-Chemical Nonequilibrium Flows, *AIAA Paper 89-0201*, 1989.
- [3] S. K. Saxena, and M. T. Nair, An Improved Roe Scheme for Real Gas Flow, *AIAA Paper 2005-587*, 2005.
- [4] E. S. G. Maciel, Analysis of Convergence Acceleration Techniques Used in Unstructured Algorithms in the Solution of Aeronautical Problems – Part I, *Proceedings of the XVIII International Congress of Mechanical Engineering (XVIII COBEM)*, Ouro Preto, MG, Brazil, 2005. [CD-ROM]
- [5] E. S. G. Maciel, Analysis of Convergence Acceleration Techniques Used in Unstructured Algorithms in the Solution of Aerospace Problems – Part II, *Proceedings of the XII Brazilian Congress of Thermal Engineering and Sciences (XII ENCIT)*, Belo Horizonte, MG, Brazil, 2008. [CD-ROM]
- [6] B. Van Leer, Flux-Vector Splitting for the Euler Equations, *Lecture Notes in Physics*, Springer Verlag, Berlin, Vol. 170, 1982, pp. 507-512.
- [7] C. Hirsch, *Numerical Computation of Internal and External Flows – Computational Methods for Inviscid and Viscous Flows*, John Wiley & Sons Ltd, 691p, 1990.
- [8] T. J. Barth, and D. C. Jespersen, The Design and Application of Upwind Schemes on Unstructured Meshes, *AIAA Paper 89-0336*, 1989.
- [9] R. N. Gupta, J. M. Yos, R. A. Thompson, and K. -P. Lee, A Review of Reaction Rates and Thermodynamic and Transport Properties for an 11-Species Air Model for Chemical and Thermal Nonequilibrium Calculations to 30000 K, *NASA RP-1232*, 1990.
- [10] E. S. G. Maciel, Relatório ao CNPq (Conselho Nacional de Desenvolvimento Científico e Tecnológico) sobre as atividades de pesquisa realizadas no período de 01/07/2008 até

- 30/06/2009 com relação ao projeto PDJ número 150143/2008-7, *Technical Report, National Council of Scientific and Technological Development (CNPq)*, São José dos Campos, SP, Brasil, 102p, 2009.
- [11] B. J. McBride, S. HeimeI, J. G. Ehlers, and S. Gordon, Thermodynamic Properties to 6000 K for 210 Substances Involving the First 18 Elements, *NASA SP-3001*, 1963.
- [12] C. R. Wilke, A Viscosity Equation for Gas Mixtures, *The Journal of Chemical Physics*, Vol. 18, No. 4, 1950, pp. 517-519.
- [13] J. C. Tannehill, D. A. Anderson, and R. H. Pletcher, *Computational Fluid Mechanics and Heat Transfer*, Second Edition, Hemisphere Publishing Corporation, 792p, 1997.
- [14] R. N. Gupta, J. M. Yos, and R. A. Thompson, A Review of Reaction Rates and Thermodynamic and Transport Properties for the 11-Species Air Model for Chemical and Thermal Nonequilibrium Calculations to 30000 K, *NASA TM-101528*, 1989.
- [15] D. Ait-Ali-Yahia, and W. G. Habashi, Finite Element Adaptive Method for Hypersonic Thermochemical Nonequilibrium Flows, *AIAA Journal*, Vol. 35, No. 8, 1997, pp. 1294-1302.
- [16] M. Liou, and C. J. Steffen Jr., A New Flux Splitting Scheme, *Journal of Computational Physics*, Vol. 107, 1993, pp. 23-39.
- [17] R. Radespiel, and N. Kroll, Accurate Flux Vector Splitting for Shocks and Shear Layers, *Journal of Computational Physics*, Vol. 121, 1995, pp. 66-78.
- [18] E. S. G. Maciel, Comparison Between the First Order Upwind Unstructured Algorithms of Steger and Warming and of Van Leer in the Solution of the Euler Equations in Two-Dimensions, *Proceedings of the XIX International Congress of Mechanical Engineering (XIX COBEM)*, Brasília, DF, Brazil, 2007.
- [19] L. N. Long, M. M. S. Khan, and H. T. Sharp, Massively Parallel Three-Dimensional Euler / Navier-Stokes Method, *AIAA Journal*, Vol. 29, No. 5, 1991, pp. 657-666.
- [20] R. W. Fox, and A. T. McDonald, *Introdução à Mecânica dos Fluidos*, Guanabara, 1988.
- [21] E. S. G. Maciel, Relatório ao Conselho Nacional de Pesquisa e Desenvolvimento Tecnológico (CNPq) sobre as Atividades de Pesquisa Desenvolvidas no Primeiro Ano de Vigência da Bolsa de Estudos para Nível DCR-IF Referente ao Processo No. 304318 / 2003-5, *Technical Report, National Council of Scientific and Technological Development (CNPq)*, Recife, PE, Brasil, 37p, 2004.
- [22] E. S. G. Maciel, Relatório ao Conselho Nacional de Pesquisa e Desenvolvimento Tecnológico (CNPq) sobre as Atividades de Pesquisa Desenvolvidas no Segundo Ano de Vigência da Bolsa de Estudos para Nível DCR-IF Referente ao Processo No. 304318 / 2003-5, *Technical Report, National Council of Scientific and Technological Development (CNPq)*, Recife, PE, Brasil, 54p, 2005.
- [23] E. S. G. Maciel, and A. P. Pimenta, Reentry Flows in Chemical Non-Equilibrium in Three-Dimensions, *WSEAS Transactions on Mathematics*, Vol. 11, Issue 3, March, 2012, pp. 227-256.